Sensors & Diagnostics

Intensity (arbitrary unit)

2θ (degree)

ZIF-8
Fc@ZIF-8

H₃C   CH₃

OH
H₃C   CH₃

ROYAL SOCIETY
OF CHEMISTRY

PAPER
Shalini Prasad *et al.*
Fc@ZeNose platform for the detection of four physiologically
relevant breath biomarkers: a case study using ethanol,
isopropanol, acetic acid, and acetone

Sensors & Diagnostics

PAPER

Check for updates

Fc@ZeNose platform for the detection of four physiologically relevant breath biomarkers: a case study using ethanol, isopropanol, acetic acid, and acetone†

Nikini Subawickrama Mallika Widanaarachchige,[a] Anirban Paul,[a] Sriram Muthukumar[b] and Shalini Prasad (iD) *[a]

Metabolomics allows the analysis of metabolites in biological samples to identify biomarkers associated with metabolic processes, and among these volatile organic compounds (VOCs) have emerged as a significant component in non-invasive diagnostics playing a crucial role in understanding physiological and pathological conditions. The changes in metabolic pathways that occur in biological systems during disease states result in the generation of VOCs as end products or intermediate products. These are then transported to the lungs *via* the circulatory system and presented into breath at the alveolar membrane. This direct link between metabolic changes and exhaled VOCs has driven growing interest in breathomics, a non-invasive approach to disease diagnosis and monitoring. Among numerous gas sensing technologies that have been explored, electrochemical sensors have demonstrated high sensitivity, cost-effectiveness, real-time monitoring, and miniaturization capabilities. In this work, we have developed a ferrocene (Fc) encapsulated zeolitic imidazole framework −8 (ZIF-8) for the detection of 4 physiologically relevant VOCs: ethanol, isopropanol, acetic acid, acetone, utilizing chronoamperometry as the transduction principle. The material characterization was performed using X-ray photoelectron spectroscopy, powder X-ray diffraction, field emission scanning electron microscopy, energy-dispersive X-ray analysis, and thermogravimetric analysis to confirm the morphological properties of Fc@ZIF-8. The dose-dependent response curves were established for each VOC, demonstrating linearity and the sensor's detection capabilities. Additionally, the sensor's accuracy was confirmed with spike and recovery experiments, achieving recovery rates within the CLSI guideline range of 80–120%.

Introduction

Metabolomics is the study of the metabolome, which consists of small molecules produced *via* cellular-level activities that are responsible for metabolic processes in organisms.[1] It has become a promising diagnostic tool in biomedical research with its ability to offer comprehensive analysis of metabolites in biological samples/fluids[2] which can be correlated to the functional status of biological systems.[3] According to the World Health Organization (WHO), a biomarker is "any substance, structure, or process that can be measured in the body or its products and influence or predict the incidence of

outcome or disease".[4] Therefore, these biomarkers can provide insight into the biological mechanism and metabolic processes. These biomarkers are often either an end-product or an intermediate product of a metabolic pathway. Therefore, detection and analysis can help us understand and create connections to the phenotype of biological systems[3] leading to disease detection and monitoring. Biomarkers expressed in different biological fluids such as blood, saliva, and urine have been utilized in clinical medicine,[5] and the analysis of these biomarkers has entered an era with a focus on the early detection of diseases and non-invasive approaches.

The search for non-invasive disease diagnostic and monitoring techniques has become a hot topic of research. Volatilomics, a subset of metabolomics,[6] has gained special attention in this area of work. Volatilomics is the study of volatile organic metabolites (VOM). These VOMs generated through metabolic events are presented into biofluids such as blood, urine, sweat, and breath. Among these, analysis of breath for VOMs has garnered special focus due to its non-

[a] *Department of Bioengineering, University of Texas at Dallas, Richardson, TX-75080, USA. E-mail: nikini.subawickramamallikawidanaara@UTDallas.edu, anirban.paul@utdallas.edu, shalini.prasad@utdallas.edu*

[b] *Enlisense LLC, Allen, TX, USA. E-mail: sriramm@enlisense.com*

invasive nature, and the opportunity to sample as often as desired compared to other biofluids. Hence, breathomics the analysis of exhaled breath has shown potential in disease diagnostics with more than 3000 volatile organic compounds (VOCs) being identified and profiled while making connections with disease-specific metabolic pathways.[2] For instance, Oyerinde et al. have shown the VOC generation in the biological systems due to oxidative stress-related diseases.[7] They have reported that the reactive oxidative species (ROS) generated due to oxidative stress interact with biological components resulting in VOC generation. Saasa et al. have reported the relationship between breath acetone levels and diabetic conditions,[8] showing the potential for a breath analysis tool for diabetes. Khokhar's extensive review has highlighted ammonia, acetone, isoprene, triethylamine, NO, and CO as potential breath biomarkers for renal disease detection.[9] Trefz et al. have reported the correlation of breath isopropanol, acetone, and pentanal and blood glucose levels showing its applicability in diabetic populations.[10] Solga et al. have studied the breath biomarkers in non-alcoholic fatty liver disease (NAFLD) and have reported ethanol, acetone, and ethane as potential biomarkers for NAFLD.[11] In another work by Dryahina et al., they have demonstrated the relationship between breath acetic acid levels and gastro-oesophageal reflux disease (GERD) reporting acetic acid's potential as a breath biomarker for GERD.[12] Therefore, endogenous VOCs are of clinical interest as they reflect the interior biology of the system. Thus, the analysis of exhaled breath holds great promise for non-invasive disease diagnosis and monitoring. Conventional non-invasive methodologies include gas chromatography, is time-consuming, requires bench space and trained personnel, and restricts it from field use.

In recent years, electrochemical sensors have emerged as a leading technology in gas sensing. Electrochemical sensors perform by converting the chemical interactions of the analyte with the sensing material into electrical signals.[13] These signals could be voltage, current, impedance, etc. Unlike optical or spectrometric methods, electrochemical sensors allow the direct, real-time measurement of gases with relatively simple and cost-effective setups. In addition, they offer high sensitivity, fast response time, and the potential for miniaturization. Electrochemical sensors also provide the opportunity to integrate/interact with other devices via the internet of things (IoT) allowing translational capabilities.[14] These features have made them an attractive contender for point-of-care diagnostic and prognostic tools. The field is constantly updating with the search for better sensitivity and selectivity towards VOCs/gases. Numerous materials have been explored for gas sensing including metal oxides, carbon-based materials, room temperature ionic liquids (RTILs), and metal organic frameworks (Table 1). Metal oxide semiconductors (MOS) have been widely used in gas sensors due to their advantages such as low cost in production, sensitivity to multiple gases,[43] long lifetime, and short response time. The working principle of these types of sensors is via the change in conductivity in the presence of oxidizing or reducing gases.[42,48] Limitations of MOS lie in its poor selectivity towards gases.[44,45] Additionally, MOS-based sensors operate at higher temperatures causing higher power consumption[47,49] which could limit the application in portable devices.

Table 1 Various sensing materials and their potential in gas sensing

Sensing material type	Material	Sensing method/working principle	Detected VOC/gas	Reference
Metal oxide semiconductors (MOS)	TiO_2	Resistance	C_3H_6O	15, 16
			H_2S	17
	ZnO	Resistance	Cl_2	18
		Resistance	C_2H_6O	19
		Resistance	NO_2	20
	SnO_2	Resistance	NO_2	21
	Mo doped SnO_2	Resistance	NH_3	22
	Co_3O_4	Resistance	H_2S	23
Room temperature ionic liquids (RTIL)	$EMIM[BF_4]$	Amperometry	NO	24
	[BMIM]Cl	Amperometry	CH_4O	25
	$([C_4mpy][NTf_2])$	Amperometry	O_2	26
Carbon-based materials	Graphene	Chemiresistance	NO_2	27
	N-rGO	Conductance	CO_2	28
		Conductance	NO	29
	LIG	Chemiresistance	NO_x	30
	PEI functionalized CNT	Resistance	CO_2	31
	MWCNT	Resistance	NH_3	32
	$g-C_3N_4$	Amperometry	C_7H_{16}	33
Metal organic framework (MOF)	ZIF-8 coated ZnO	Chemiresistance	CH_2O	34
	SnO_2/ZIF-8	Resistance	NO_2	35
	AuNP@ZIF-8	Amperometry	C_5H_8	36
	Fc@ZIF-8	Amperometry	NH_3	37
			C_3H_6O	Current work
			C_2H_6O	
			$C_2H_4O_2$	
			C_3H_8O	

Several carbon-based materials have been explored as possible gas-sensing materials. For instance, graphene has been looked into as a gas-sensing material due to its unique structure and low noise.[38] On the other hand, carbon nanotubes (CNTs) have been explored as another material for gas sensing purposes due to their structure and high sensitivity.[38] The hollow structure of the tubes allows for high material absorption.[39] Unfortunately, this advantage comes along with the limitation of long recovery time.[40] Doping has become an area of research to overcome these challenges.[40] Room temperature ionic liquids (RTILs) are another material of interest in gas sensing research. Their high intrinsic conductivity, wide electrochemical window, and high thermal stability have made them ideal candidates for gas sensing.[41] One of the challenges when implementing RTILs in gas sensing systems has been reported to be the difficulty in gas diffusion through the liquid due to high viscosity.

Metal organic frameworks (MOFs) have garnered special attention in gas sensing platforms (Table 1) with their ability to overcome many of the challenges other materials are present with. MOFs are a class of crystalline porous nanomaterials that are self-assembled with inorganic metal ions/clusters and organic ligands.[41–44] They have gained widespread attention as a sensing material due to unique features such as large surface area, tunable porosity/geometry, reversible uptake and release of analytes, thermal stability, and abundance of active sites.[41,43,45] The high selectivity towards analytes that comes with large surface area and tunable pore size, and the storage capabilities allowed by the porous structure have made MOFs a material of choice in gas sensing. Additionally, MOFs achieve their selectivity towards analytes/gases by their pore size, modification of clusters, and functionalization of the ligands.[44] These unique features have made MOF an interesting choice of material in breath VOC detection. Zinc imidazole framework 8 (ZIF-8), a subclass of zeolitic MOFs has shown excellent electrochemical properties making it a fine transduction material in electrochemical sensors.[46] Nanoparticle encapsulated ZIF-8 has shown enhanced electrochemical properties highlighting its potential in electrochemical sensing.[46,47]

In this work, we have developed a metal–organic framework (MOF)-based sensor utilizing ZIF-8, a subclass of zeolitic MOFs, as the sensing platform. Ferrocene, a redox-active molecule, has been encapsulated within the ZIF-8 cavity to enhance the electrochemical properties of the sensor. The sensor has been tested for its ability to detect and measure four key VOCs: ethanol (100 ppm–1500 ppm), isopropanol (IPA) (20 ppm–200 ppm), acetic acid (1 ppm–10 ppm), acetone (50 ppm–1000 ppm). These VOCs were selected based on their reported physiological relevance and prevalence across multiple disease categories, as well as their potential to highlight the sensor's versatility and sensitivity. This study demonstrates the material's sensing capabilities, electrochemical transduction mechanism, and overall detection capabilities in a proof-of-concept setting.

Experimental section

Materials and methods

Analytical grade ferrocene (Fc, 98%), zinc nitrate, 2-methylimidazole, and methanol were purchased from Sigma-Aldrich for the synthesis of the Fc@ZIF-8 nanocomposite. Screen-printed gold electrodes, featuring gold working and counter electrodes as well as silver reference electrodes, were sourced from Metrohm AG. Room temperature ionic liquid (RTIL) 1-butyl-3-methylimidazolium tetrafluoroborate [BMIM][BF$_4$] (>98%), 5% Nafion in a mixture of lower aliphatic alcohols, and 99.5% anhydrous 1-methyl-2-pyrrolidinone were purchased from Sigma-Aldrich for sensor fabrication work. Acetic acid (>99.99%) was purchased from Sigma-Aldrich, while 70% v/v isopropanol, 95.27% anhydrous ethanol, and acetone solutions were obtained from Fisher Chemicals. GasTec validation tubes were purchased from GASTEC International for the concentration validation of the VOCs: acetone, ethanol, acetic acid, and isopropanol. A bubbler system was set up in a fume hood with an in-house nitrogen input for the generation of VOCs.

Synthesis of fc@ZIF-8

The synthesis of Fc@ZIF-8 was carried out using a protocol adapted from a previously established procedure.[48,49] The synthesis of Fc@ZIF-8 was carried out through the following steps. First, two solutions were prepared: solution 1, consisting of 7.2928 g of zinc nitrate (Zn(NO$_3$)$_2$) dissolved in 200 mL of ethanol to yield a 133 mM solution, and solution 2, a 1 M solution of 2-methylimidazole prepared by dissolving 8.211 g of 2-methylimidazole in 100 mL of methanol. To solution 1, 20 mmol of ferrocene (3.7208 g) was added, resulting in a pale-yellow solution. Solutions 1 and 2 were then combined, and the beaker was covered with aluminum foil to prevent evaporation, followed by overnight stirring. The mixture turned cloudy with visible fine particles, indicating the encapsulation of ferrocene within the ZIF-8 structure. The reaction mixture was left undisturbed to allow the particles to settle. The supernatant was carefully removed by pipetting, ensuring that the precipitate remained undisturbed. The collected precipitate was transferred to a 10 mL centrifuge tube and centrifuged at 6000 rpm for 10 minutes. The supernatant was discarded, and the precipitate was resuspended in methanol before being recentrifuged. This washing procedure was repeated five times. Finally, the nanocomposite was transferred to a glass Petri dish, covered with aluminum foil, and dried under vacuum overnight. The synthesized Fc@ZIF-8 was stored at 4 °C for further use. The synthesis procedure is demonstrated in Fig. S1.†

Material characterization

The synthesized Fc@ZIF-8 nanocomposite was characterized using several analytical techniques. Powder XRD was performed in Siemens D500 PXRD instrument with a 5°

min⁻¹ scan rate. X-ray photoelectron spectroscopy (XPS) was conducted using PerkinElmer Phi 560 XPS system to investigate the composition and chemical states of the nanocomposite. Scanning electron microscopy (SEM) and elemental mapping (EDS) were employed to observe the surface morphology of the material using the Hitachi S-3000NSEM/EDS system. These characterization methods provided comprehensive information about the structural, chemical, and morphological properties of the synthesized Fc@ZIF-8. Thermogravimetric analysis (TGA) has been performed to understand the thermal stability of the as-synthesized material, and it was done in the TA SDT-Q600 simultaneous TGA system. Electrochemical experiments were performed in Gamry Potentiostat.

Sensor preparation and electrochemical techniques

The screen-printed electrodes were procured from Metrohm AG. The concentric 3-electrode system consists of gold working and counter electrodes and a silver reference electrode. 1 mg of synthesized Fc@ZIF-8 was dissolved in 50 μL of 1-methyl-2-pyrrolidinone and sonicated to form a slurry. A mixture of 5% Nafion and room temperature ionic liquid (RTIL) [BMIM][BF₄] was prepared in a 1:5 ratio and sonicated to ensure uniformity. For electrode modification, 10 μL of the prepared Fc@ZIF-8 slurry was drop-cast onto the gold working electrode and allowed to dry, serving as the transducer for the electrochemical platform. Subsequently, 10 μL of the RTIL solution was drop-cast over all three electrodes to form the electrolyte layer in the system (Fig. S3†). The electrode was then placed in the electrochemical sensing setup. A bubbler system was prepared with an in-house Nitrogen input of over 95% purity.

The stock solutions of acetone, isopropanol, ethanol, and acetic acid were prepared at varying concentrations for VOC generation via nitrogen (N₂) bubbling. GasTec validation tubes were used to validate generated VOC concentrations (Fig. S4†). The following concentration ranges were established and validated for each VOC: acetone (100 ppm to 1000 ppm), isopropanol (20 ppm to 200 ppm), acetic acid (1 ppm to 10 ppm), and ethanol (100 ppm to 1500 ppm). These validated concentration ranges were used in electrochemical testing to assess the sensor's response to different VOC levels. The experimental setup has been described in Fig. S2.† Cyclic voltammetry (CV) was employed to select the appropriate bias potential for each VOC by scanning a potential range from −1 V to +1 V. Following bias potential selection, double potential chronoamperometry (DPCA) was performed to investigate the dose-dependent response at the electrode–Fc@ZIF-8 interface for each VOC. The current output was measured at a selected time point for each VOC and used to construct a calibrated dose-dependent response curve. Electrochemical impedance spectroscopy (EIS) was conducted with a DC bias of 0 V to establish a baseline for nitrogen (N₂) and the low, medium, and high concentrations of each VOC, enabling an analysis of the double layer

characteristics. To evaluate the sensor performance in a complex matrix, chronoamperometry was performed using un-spiked and VOC-spiked simulated samples. Diffusion-limited currents were extracted to assess the sensor's ability to distinguish target VOC in a complex matrix. The circuit fitting was performed using Zview software while all statistical analyses were performed with GraphPad. All electrochemical measurements were carried out using a Gamry potentiostat. Sensor stability testing was performed with open circuit potential (OCP) measurements and baseline EIS measurements. A humidity assessment was performed to evaluate the sensor stability under humid conditions introduced by the bubbler-based VOC sample collection.

Results and discussion

Material characterization

The synthesized nanomaterial Fc@ZIF-8 was subjected to comprehensive physicochemical characterization to elucidate its structural integrity and compositional profile following ferrocene encapsulation within the ZIF-8 framework. X-ray photoelectron spectroscopy (XPS) analysis revealed the elemental composition of Fc@ZIF-8, with the full scan, depicted in Fig. 1(a) demonstrating the presence of Zn (2p), O (1s), N (1s), and C (1s) signals. Specifically, the Zn 2p spectrum exhibited characteristic peaks at 1026.02 eV for Zn 2p₍₃/₂₎ and 1049.20 eV for Zn 2p₍₁/₂₎, with the peak separation of 23.18 eV confirming the Zn 2p oxidation state. A notable shift in the C–C peak position to 288.2 eV was observed, attributed to the structural modifications induced by ferrocene encapsulation, which causes framework bond inflation. These spectral alterations substantiate the successful formation of the Fc@ZIF-8 composite. O 1s peak at 532.32 eV and N 1s peak at 399.5 eV depicts standard ZIF-8 architecture. Powder X-ray diffraction (PXRD) was employed for phase characterization of the vacuum-dried samples. The diffraction pattern of Fc@ZIF-8, depicted in Fig. 1(b), was compared against control ZIF-8 (JCPDS 00-062-1030). The comparative analysis demonstrated peak overlap between Fc@ZIF-8 and ZIF-8, indicating preservation of the crystalline structure despite ferrocene encapsulation. Notably, the absence of characteristic ferrocene diffraction peaks in the Fc@ZIF-8 pattern suggests molecular-level dispersion of ferrocene throughout the composite matrix. The synthesized ZIF-8 patterns were further validated against simulated ZIF-8 (JCPDS 00-062-1030; $a = b = c = 17.0116$ Å; $\alpha = \beta = \gamma = 90°$), confirming the structural purity of the synthesized ZIF-8 framework. Additional comparison with simulated ferrocene diffraction data (JCPDS 29-1711; $a = b = c = 17.0116$ Å; $\alpha = 90°$, $\beta = 121.05°$ (8°), $\gamma = 90°$) revealed the absence of ferrocene's characteristic peaks in Fc@ZIF-8, providing further evidence of complete ferrocene encapsulation within the ZIF-8 matrix. These findings confirm that the electrochemical nose system maintains the cubic crystalline architecture of ZIF-8 despite ferrocene incorporation. Field
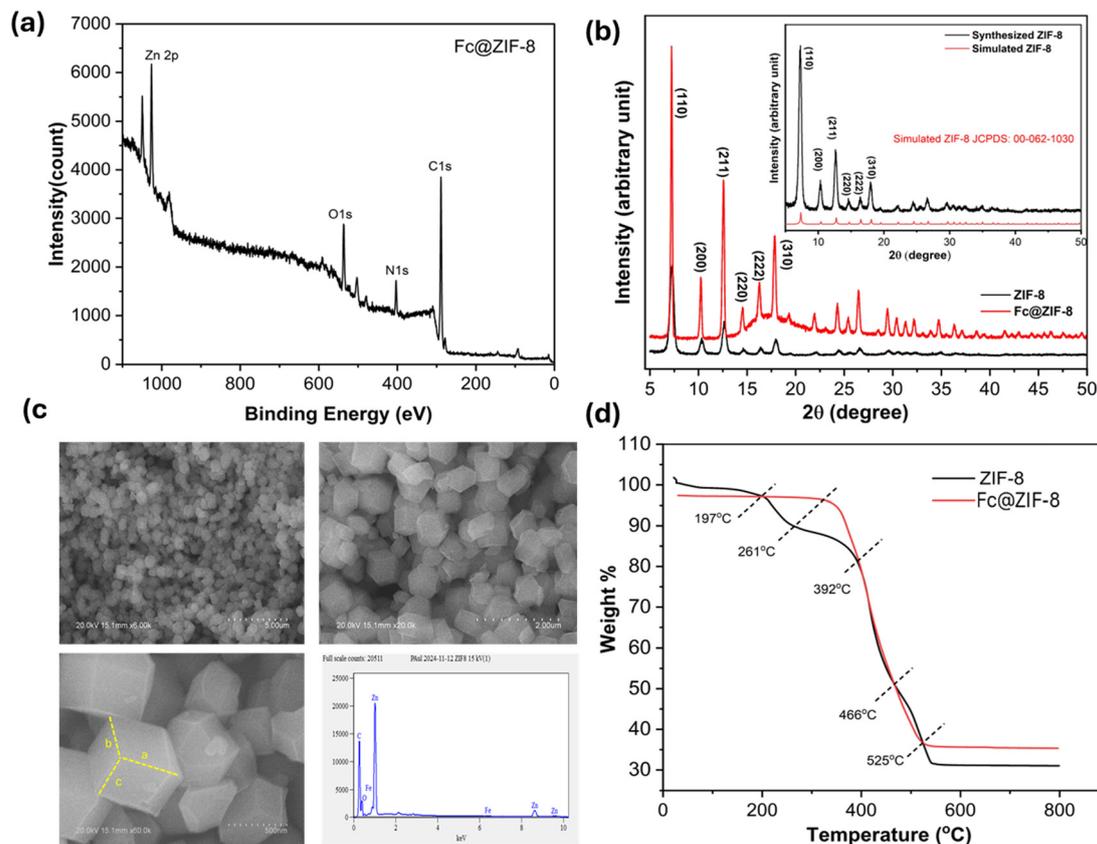
Fig. 1 (a) XPS full spectrum of synthesized Fc@ZIF-8, showing major ZIF-8 peaks. (b) P-XRD spectra of synthesized material: Fc@ZIF-8, compared with pristine ZIF-8, showing the presence of ZIF-8 fingerprint peaks. The synthesized bare ZIF-8 P-XRD spectra are compared with standard ZIF-8, JCPDS: 00-062-1030, showing inset. (c) FE-SEM morphological output of synthesized material showing the typical cubic morphology with EDS mapping. (d) TGA comparison between ZIF-8 and Fc@ZIF-8 shows the thermal stability of the as-synthesized material.

emission scanning electron microscopy (FESEM) was utilized to examine the morphological characteristics of Fc@ZIF-8. Micrographs depicted in Fig. 1(c) reveal homogeneous crystal structures across multiple magnifications. The preservation of ZIF-8's inherent cubic polyhedral morphology after ferrocene encapsulation corroborates the PXRD results, confirming that ferrocene incorporation occurs homogeneously within the ZIF-8 lattice without compromising its structural integrity. The cubic polyhedral morphology observed aligns with previously reported literature on ZIF-8-based materials.

Energy-dispersive X-ray analysis (EDAX) was performed to quantify and confirm the elemental distribution of encapsulated ferrocene. The spectra are depicted in Fig. 1(c); results indicated a ferrocene content of 1% (by weight) within the Fc@ZIF-8 nanocomposite, validating the successful incorporation of ferrocene within the ZIF-8 framework. Thermogravimetric analysis (TGA) conducted under argon atmosphere provided insights into the thermal stability of the synthesized materials. Comparative analysis between pristine ZIF-8 and the Fc@ZIF-8 composite revealed similar deformation profiles but with distinct degradation kinetics. Pristine ZIF-8 exhibited approximately 50% mass loss by 434 °C, whereas the Fc@ZIF-8 composite demonstrated enhanced thermal

resistance, with 90% mass loss occurring between 434 °C and 517 °C. This differential thermal behaviour suggests a sequential degradation mechanism: initial decomposition of the ZIF-8 framework followed by degradation of the encapsulated ferrocene species. The result is depicted in Fig. 1(d). The altered thermal profile provides further evidence of successful ferrocene encapsulation and indicates substantial thermal stability of the Fc@ZIF-8 composite. The characterization data suggests the formation of ZIF-8, and the major output is dominated by ZIF-8 output, especially P-XRD, and XPS, and does not show any output of Ferrocene as the amount of Ferrocene encapsulated is way less than the stoichiometric abundance of pristine ZIF-8. Although we have obtained the signal of Ferrocene in the Fc@ZIF-8 composite by performing FT-IR spectroscopy of pristine ferrocene powder and Fc@ZIF-8, depicted in Fig. S5,† the result shows the presence of fingerprint Ferrocene peaks in Fc@ZIF-8.[37] The peak at 422 cm^{-1} represents Fe–C stretching, usually visible in 400–500 cm^{-1} range, and also appeared at 466 cm^{-1} in pristine Ferrocene. The other two important peaks at 757 cm^{-1} and 1146 cm^{-1} represent cyclopentadienyl (Cp) ring vibrations, got shifted from its original stretching output, depicted in pristine Ferrocene at 808 cm^{-1} and 1104 cm^{-1}s proves the encapsulation of the species, showing peak shifting due to trapped in ZIF-8 motif.

Application of the Fc@ZIF-8 platform for the detection of VOCs

Studies have demonstrated the potential of Fc@ZIF-8 as an effective nanocomposite for electrochemical sensing applications highlighting its excellent electrocatalytic properties, high surface area, and stable encapsulation of ferrocene, which enhance electron transfer and facilitate selective detection of target analytes. Building on this foundation, we have employed the Fc@ZIF-8 platform for the electrochemical detection of four physiologically relevant VOCs—ethanol, acetone, acetic acid, and isopropanol—due to their clinical significance in various diseases. Electrochemical sensing is particularly well-suited for point-of-care and portable diagnostic devices, offering advantages such as high sensitivity, rapid response, and the ability to function in miniaturized and field-deployable formats. The methodology enables efficient diffusion of analytes toward the electrode interface, ensuring robust and reproducible detection in gas sensing applications.

To achieve this, we utilized the Metrohm 220AT screen-printed electrode, designed as a three-electrode system consisting of a gold working electrode (WE), a gold counter electrode (CE), and an Ag/AgCl reference electrode (RE). The WE was modified with 0.5 µL of Fc@ZIF-8 slurry, which was allowed to dry at room temperature. For electrochemical transduction, RTIL [BMIM][BF4] was used as the electrolyte, with 10 µL drop-cast to ensure complete coverage of all three electrodes. The electrode was subsequently spin-coated at 900 rpm for 15 s to remove excess electrolyte and create a uniform thin film of RTIL, ensuring proper circuit completion. This RTIL-Fc@ZIF-8 layer facilitates the efficient diffusion of VOCs to the electrode surface, enhancing signal transduction and minimizing interference.

A cyclic voltammetry scan rate variation study has been performed by utilizing different scan rates from 50–400 mV s^{-1} showing a steady increase of anodic and cathodic current, depicted in Fig. S6.† The result depicts smooth charge transfer across the electrochemical double layer, responsive to the standard Randles–Sevcik equation for scan rate response. Sensor stability was validated with open circuit potential (OCP) measurements and the results showed the stabilization of the sensor at approximately 350 s showing the sensor's electrochemical stability over time. Upon EIS analysis of $N = 15$, the bode plot exhibited minimal variance indicating high sensor stability (Fig. S7†). All experiments in this study were performed using VOC samples generated through a bubbler setup which inherently introduces moisture to the test samples. Therefore, a humidity assessment was conducted using an in-lab made setup (Fig. S8A†). The humidity of the bubbler generated sample was measured to be 67%. Sensor stability upon sample exposure was assessed by performing chronoamperometry using low and high concentrations of ethanol samples as representative samples. 10 cycles of Chronoamperometry were repeated and results showed minimal variation in response (Fig. S8B†).

This showed that within the scope of this current work, sensor response remains stable under humid conditions similar to breath samples.

Following sensor stability verification, electrochemical studies were then conducted for each VOC to evaluate their interaction with the modified electrode interface. Cyclic voltammetry has been performed to understand the interactions of the VOC with the modified electrode interface. EIS was performed to understand the sensor microenvironment and the diffusion characteristics. Chronoamperometry has been employed as the transduction principle to study the diffusion characteristics across the electrode–electrolyte interface governed by Fick's Law. The semipermeable membrane-like behaviour of the electrode–electrolyte interface creates a concentration gradient facilitating the diffusion of the VOC.

$$j = -D\frac{\partial C}{\partial X} \quad (1)$$

where j is the diffusion flux, D is the diffusion coefficient, X is the position, and C is the concentration of the analyte. Following the Cottrell Equation, the current produced by the electrode system upon exposure to the analyte is attributed to the diffusion happening at the interface.

$$i = \frac{nFAc_j^o\sqrt{Dj}}{\sqrt{\pi t}} \quad (2)$$

where i is the diffusion current, c_j^o is the concentration of the diffused species and t is the time.

Ethanol

The experiments were performed for ethanol concentrations ranging from 100 ppm to 1500 ppm which were allowed for validation by GasTec validation tubes (Fig. S4†). Primarily, a cyclic voltammetry scan was performed from −1 V to +1 V at a scan rate of 100 mV s^{-1}. Three significant peaks were observed with dose-dependent trends and potentials surrounding all peaks were analysed for the dose-dependency and linearity in current output. 0.9 V was selected as the bias potential for the following chronoamperometric study due to the dose-dependent nature at the selected potential and the highest linearity of $R^2 = 0.897$ in current output compared to other potentials (Fig. 2A).

Double potential chronoamperometry was performed at the selected potential for 60s. The transient anodic diffusion current was extracted at 3 s and Δ current output was calculated for each dose. The calibrated dose–response curve was built using a logarithmic scale fitting with three parameters and an R^2 value of 0.989 was obtained (Fig. 2B). The experiments were performed with $n = 3$ repeats. The results show increasing Δ current output with increasing concentrations with a significance of $p = 0.0009$, $p = 0.03$, $p = 0.0001$ between the doses 100–500 ppm, 500–1500 ppm, and 100–1500 ppm, respectively.
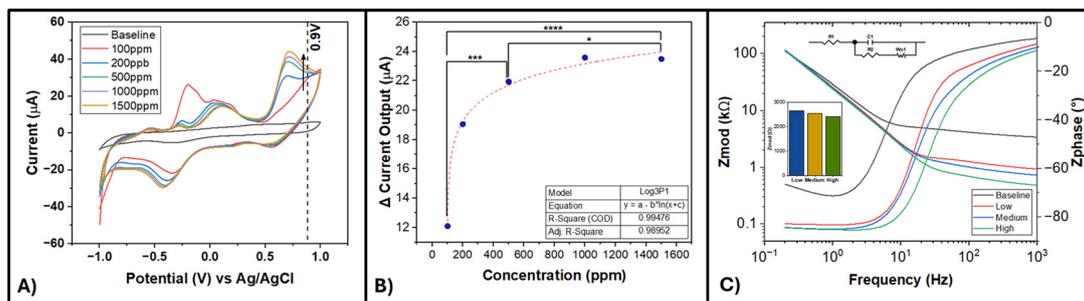
Fig. 2 A) Cyclic voltammetry performed from −1 V to +1 V for ethanol concentrations ranging from 100 ppm to 1500 ppm. B) Calibrated-dose–response curve for ethanol concentration ranging from 100–1500 ppm C) Bode plots for ethanol detection from 100–1500 ppm. Extracted Z_{mod} change at 10 Hz depicting change in impedance low, medium and high concentrations of ethanol (inset).

Electrochemical impedance spectroscopy (EIS) was conducted to analyse the electrochemical characteristics of the sensor microenvironment. The sensor response was evaluated at three concentrations: low (100 ppm), medium (500 ppm), and high (1500 ppm). EIS measurements were performed over a frequency range of 0.1 Hz to 1 MHz at a DC voltage of 0.0 V. The corresponding Bode plot is presented in Fig. 2C, while the extracted Z_{mod} values at 10 Hz are shown in the inset of Fig. 2(C). 10 Hz was picked for Z_{mod} extraction due to the high goodness of fit shown compared to other frequencies (Table S1†). A decrease in impedance was observed with increasing analyte concentration, which can be attributed to an increase in the system's capacitance. Notably, this increase in capacitance aligns with the cyclic voltammetry (CV) response. The limit of detection (LOD) for ethanol was statistically determined to be 2.95 ppm. The LOD calculations were performed using the formula

$$\text{LOD} = \frac{3\sigma}{S} \tag{3}$$

where σ stands for standard deviation and S stands for the slope of the calibration curve.

Isopropanol

The electrochemical response of the sensor was evaluated for isopropanol concentrations ranging from 20 ppm to 200 ppm, validated using GasTec tubes (Fig. S4†). Cyclic voltammetry (CV) was initially conducted within a potential

window of −1 V to +1 V at a 100 mV s^{-1} scan rate, revealing three prominent peaks that exhibited a dose-dependent trend. Among the tested potentials, 0.15 V was selected as the bias potential for chronoamperometric studies, as it demonstrated the strongest dose-dependent response and the highest linearity ($R^2 = 0.954$) in the current output (Fig. 3A).

Double-potential chronoamperometry was performed at the chosen potential over 60s, with the transient cathodic diffusion current extracted at 5 s. The resulting Δ current output was plotted against concentration, and a calibrated dose–response curve was generated using a nonlinear cubic fit, achieving an R^2 value of 0.99 (Fig. 3B). Each experiment was conducted in triplicate ($n = 3$) to ensure reproducibility. An increase in Δ current output was observed with increasing isopropanol concentrations, with significance values of $p = 0.034$, $p = 0.02$ for comparisons between 20–100 ppm and 20 ppm–200 ppm, respectively.

To further investigate the electrochemical characteristics of the sensor microenvironment, EIS measurements were also conducted with isopropanol. The sensor response was evaluated at three different concentrations—low (20 ppm), medium (100 ppm), and high (200 ppm). Measurements were carried out over a frequency range of 0.1 Hz to 1 MHz at a DC bias of 0.0 V. The resulting Bode plot is illustrated in Fig. 3C, with Z_{mod} values at 5 Hz extracted and presented in the inset. Compared to other frequencies at 5 Hz the best goodness of fit was observed (Table S1†). An increase in
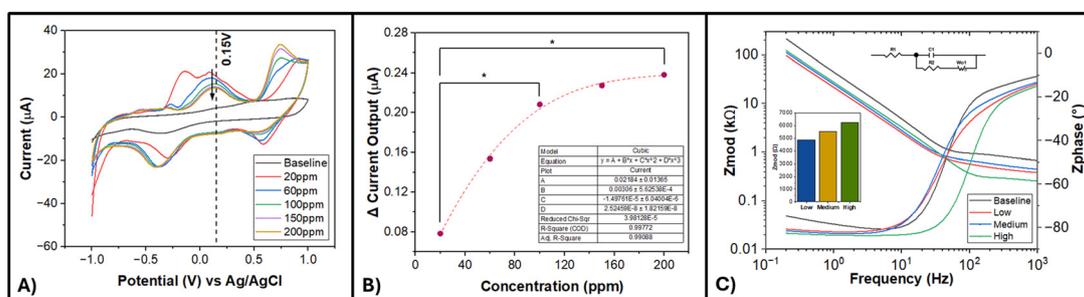

Fig. 3 A) Cyclic voltammetry performed from −1 V to +1 V for isopropanol concentrations ranging from 20 ppm to 200 ppm. B) Calibrated-dose–response curve for isopropanol concentration ranging from 20–200 ppm C) Bode plots for isopropanol detection from 20–2000 ppm. Extracted Z_{mod} change at 10 Hz depicting change in impedance low, medium and high concentrations of isopropanol (inset).

impedance was observed with increasing isopropanol concentration, indicating a reduction in system capacitance. The observed decrease in capacitance is also reflected in the cyclic voltammetry (CV) results, reinforcing the influence of isopropanol concentration on the electrochemical properties of the sensor. The calculated LOD for isopropanol was found to be 34.12 ppm (formula (3)).

Acetic acid

The experiments were conducted for acetic acid concentrations ranging from 1 ppm to 10 ppm, validated using GasTec validation tubes (Fig. S4†). Initially, cyclic voltammetry was performed within a potential window of −1 V to +1 V at a scan rate of 100 mV s^{-1}. Although several peaks were exhibited only one peak showed a clear dose-dependent trend. The surrounding potentials for that peak were analysed for current output linearity. Among these, 0.22 V was chosen as the bias potential for the chronoamperometric study, as it demonstrated a pronounced dose-dependent response and the highest linearity, with an R^2 value of 0.887 (Fig. 4A).

Following this, double-potential chronoamperometry was carried out at the selected potential for 60s, with transient anodic diffusion current extracted at 5 s. The Δ current output was calculated for each dose, and a calibrated dose–response curve was generated using a cubic nonlinear fit, yielding an R^2 value of 0.963 (Fig. 4B). The study was conducted with $n = 3$ repeats. The results indicate a relative increase in Δ current output with rising acetic acid concentrations, with statistical significance of $p = 0.005$, and $p = 0.0006$, between the doses 7 ppm–10 ppm, and 1 ppm–10 ppm, respectively (Fig. 4(B)).

EIS analysis was also performed with acetic acid to assess its impact on the sensor microenvironment. The sensor response was recorded at three concentration levels 1 ppm, 5 ppm, and 10 ppm. Measurements were conducted across a frequency range of 0.1 Hz to 1 MHz under a DC bias of 0.0 V. The corresponding Bode plot is illustrated in Fig. 4C, with Z_{mod} values at 5 Hz extracted and detailed in the inset. At 5 Hz the best goodness of fit was observed compared to other frequencies tested (Table S1†). The data revealed a

progressive decline in impedance with increasing acetic acid concentration, suggesting an enhancement in system capacitance. This behaviour indicates greater charge storage capability at higher analyte levels, as further corroborated by the cyclic voltammetry (CV) results. An LOD of 2.29 ppm was statistically calculated for acetic acid (formula (3)).

Acetone

Experiments for acetone detection were conducted across a concentration range of 50 ppm to 1000 ppm, with GasTec validation tubes used for verification (Fig. S4†). Cyclic voltammetry was performed from −1 V to +1 V at a scan rate of 100 mV s^{-1}, revealing two key peaks that exhibited dose-dependent behaviour. The potential surrounding these peaks was assessed for current response linearity, leading to the selection of 0.1 V as the bias potential for subsequent chronoamperometric studies. This potential demonstrated a dose-dependent response with the highest linearity, with an R^2 value of 0.868 (Fig. 5(A)).

Double-potential chronoamperometry was then performed at the chosen potential over a 60s period, with transient anodic diffusion current extracted at 2 s. The Δ current output was determined for each concentration, and a calibrated dose–response curve was constructed using a three-parameter logarithmic fit, achieving an R^2 value of 0.997 (Fig. 5(B)). Each experiment was repeated three times ($n = 3$). The results confirmed a clear dose-dependent increase in Δ current output, with statistical significance of $p = 0.043$, $p = 0.006$, $p = 0.005$, observed between the concentration pairs 50–200 ppm, 50–500 ppm, and 50–1000 ppm, respectively.

To further evaluate the sensor's electrochemical behaviour, EIS was conducted using acetone. Sensor performance was assessed across three concentration levels 50 ppm, 200 ppm, and 1000 ppm. The impedance response was recorded over a frequency range of 0.1 Hz to 1 MHz with a DC bias of 0.0 V. The resulting Bode plot is shown in Fig. 5(C), with Z_{mod} values at 5 Hz extracted and highlighted in the inset. The selection of 5 Hz for extraction was based on the highest goodness of fit it showed, compared to other frequencies (Table S1†). A progressive rise in impedance was
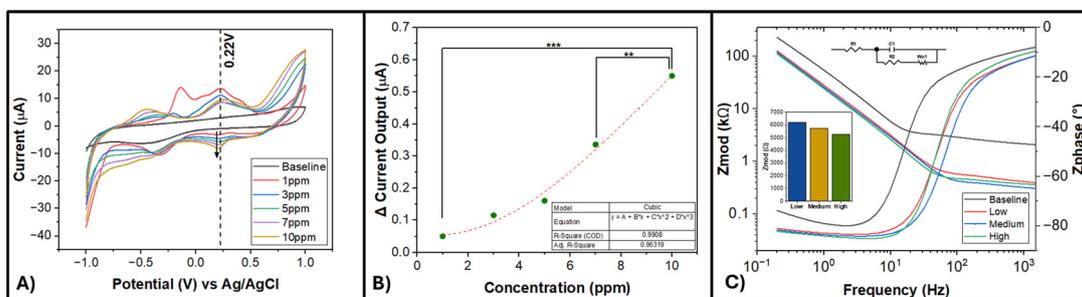

Fig. 4 A) Cyclic voltammetry performed from −1 V to +1 V for acetic acid concentrations ranging from 1 ppm to 10 ppm. B) Calibrated-dose–response curve for acetic acid concentration ranging from 1–10 ppm C) Bode plots for acetic acid detection from 1–10 ppm. Extracted Z_{mod} change at 10 Hz depicting change in impedance low, medium and high concentrations of acetic acid (inset).
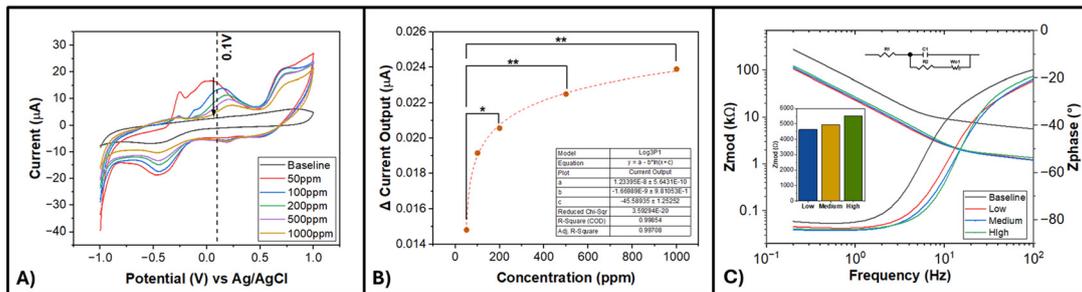
Fig. 5 A) Cyclic voltammetry performed from −1 V to +1 V for acetone concentrations ranging from 100 ppm to 1500 ppm. B) Calibrated-dose–response curve for acetone concentration ranging from 100–1500 ppm C) Bode plots for acetone detection from 100–1500 ppm. Extracted Z_{mod} change at 10 Hz depicting change in impedance low, medium and high concentrations of acetone (inset).

observed with increasing acetone concentration, indicating a reduction in system capacitance. This suggests a diminished charge storage capability at higher analyte levels, aligning with trends observed in cyclic voltammetry (CV) measurements. Statistical evaluation of dose–response data yielded an LOD of 0.214 ppm for acetone.

Spike and recovery study of the VOCs

The developed biosensor was further evaluated by testing the same concentration ranges used for calibration. In this case, the bubbler solutions were made following the exact procedure for the calibration tests, but the secondary validation was not done with the GasTec validation tubes. The sensor response was then measured, and concentrations were estimated using the previously built dose-dependent response curve. The percent recovery was then calculated to assess the accuracy of the sensor (Fig. 6). For ethanol, the recovery ranged from 83% to 110%, while IPA showed a recovery between 83% and 116%. Similarly, acetone exhibited a recovery range of 88% to 105%, while acetic acid produced a recovery range of 85% to 115%, all of which fell within the biosensor's operational range (CLSI guideline 80–120% recovery). The overall recovery percentages highlight the reproducibility of the sensor's data and further validate the accuracy of the constructed dose–response curve.

Preliminary specificity assessment

To assess the sensor's response in a more realistic environment, a preliminary experiment was conducted with simulated samples. Chronoamperometry was performed for the 4 VOC under two conditions: un-spiked simulated samples and VOC spiked simulated samples. Spiking concentrations were maintained at ppm for ethanol, ppm for isopropanol, ppm acetic acid, and ppm for acetone. Transient diffusion currents were extracted at the respective time points for each VOC and a comparison was done between the two conditions (Fig. S9†).

In all four cases, the VOC spiked samples had a significant current response relative to the un-spiked sample indicating the sensor's ability to distinguish the target VOC even within a simulated matrix. Statistical analysis revealed

that the difference between the two conditions was highly significant with a p-value of 0.0001 for all 4 VOCs (Fig. S9†). These results provide preliminary evidence and indicate specificity and the reliable detection of the developed sensor towards ethanol, isopropanol, acetic acid, and acetone.

The results obtained from the experiments performed show the developed sensor's ability to detect the 4 VOCs: ethanol, isopropanol, acetic acid, and acetone in the tested ranges. The spike and recovery further validated the dose–response curves for each VOC. A comparison between the 4 VOCs was made to rank the modified electrode–electrolyte interface's selectivity towards each (Table 2).

With all 4 VOCs showing excellent R^2 values in their dose-dependent-response and recovery percentages falling within the CLSI guideline ranges, the p-value/significant difference between the lowest and the highest dose of the testing range was selected to rank the interactions of the analytes with the modified electrode–electrolyte interface. It should be noted that this work showcases the potential of the Fc@ZIF-8 modified electrode for detecting ethanol, isopropanol, acetic acid, and acetone. We have also evaluated the EIS circuit by fitting the data using Z-view
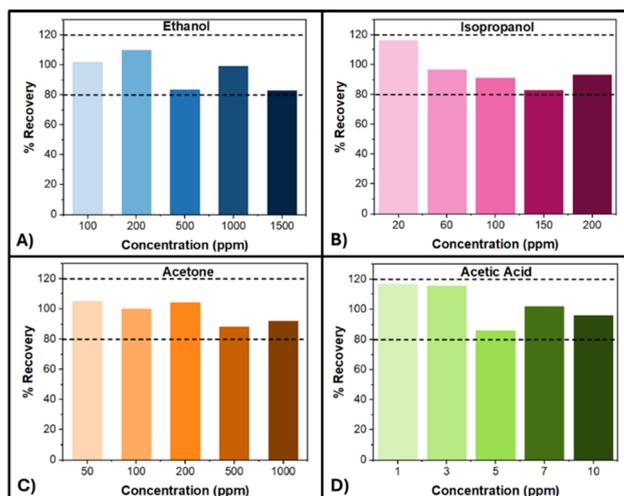

Fig. 6 Percent recovery calculated for the recovered concentrations of ethanol (A) isopropanol (B) acetone (C) and acetic acid (D) using established dose response curves.

Table 2 Comparison of sensor response to ethanol, isopropanol, acetic acid and acetone

VOC	R^2 value	P-Value (low-high)	% recovery (80–120%) Y/N	Rank
Ethanol	0.989	****	Y	1
Isopropanol	0.99	*	Y	4
Acetic acid	0.963	***	Y	2
Acetone	0.997	**	Y	3

[ns: p-value > 0.05, *: $P \le 0.05$, **: $P \le 0.01$, ***: $P \le 0.001$, ****: P 0.0001.

software. The results suggest that modified Randle's circuit depicted in Fig. 2(C), 3(C), 4(C) and 5(C) provided the best fit across all tested VOCs. The Warburg component which represents diffusion behaviour points out bulk diffusion of VOCs to the electrode–electrolyte interface, and justifies the dynamic diffusion characteristics, captured by chronoamperometric responses. We have also compared the frequency-dependent behaviour of each VOC, showing the linearity in dose dependency (Table S1†). The frequency domain at 10 Hz is mostly dominated by Warburg and charge transfer resistance components, both pointing out the fundamentals of the fabricated sensor mechanism, explained throughout.

Limits of detection (LODs) were determined for each of the four VOCs based on statistical analysis of the sensor response. The LOD for acetone was found to be within the clinically relevant sub-ppm range demonstrating the sensor's capability for sensitive detection of acetone. For ethanol, isopropanol, and acetic acid, calculated LODs are higher than typical concentrations observed in healthy breath. However, these results serve as a crucial proof-of-concept demonstrating the potential of the Fc@ZIF-8 sensing chemistry and its ability to successfully detect the reported VOCs. Future work will focus on improving the sensitivity of the sensing material to bring the detection limits into the sub-ppb range.

This work is a proof-of-concept showing the potential of Fc@ZIF-8-based electrochemical sensors in VOC detection. The results show the sensor's ability to detect ethanol, isopropanol, acetic acid, and acetone. The preliminary evaluation of sensor response in simulated samples shows a statistically significant distinction between un-spiked and spiked samples highlighting the platform's potential for selective detection in complex environments. However, a comprehensive assessment of specificity and selectivity with real breath samples remains an important next step. Future efforts will focus on systematically investigating cross-reactivity and matrix effects to ensure robust and reliable performance in real-world breath analysis applications. Further research needs to be done on evaluating multiplexing capabilities.

Conclusions

Breathomics is an emerging technology owing to its non-invasive nature and diagnostic capabilities. Breath profiling has shown breath biomarkers such as volatile organic compounds (VOCs) can be used to understand the internal health of an organism due to their link to metabolic processes. Among such VOCs, it has been reported ethanol, isopropanol, acetic acid, and acetone to be present in several metabolic diseases, chronic diseases, and respiratory diseases. In this work, we have developed an electrochemical sensor with Fc@ZIF-8 modified electrode. The synthesized nanocomposite is characterized by the standard techniques: XPS, PXRD, FESEM, EDAX, and TGA. Chronoamperometry is leveraged as the transduction principle to evaluate the diffusion kinetics of the analytes at the sensor interface. The study establishes a proof of concept for a MOF-based electrochemical sensing platform capable of detecting the 4 VOCs: ethanol, isopropanol, acetic acid, and acetone. The demonstrated detection ranges validate the sensing chemistry and material response providing a strong foundation for further refinement. Moving forward, sensor optimization efforts will focus on lowering the detection limits to match the physiological ranges. Further work needs to be done to evaluate cross-reactivity, multiplexing, and developing a dose-dependent response utilizing real breath samples.

Data availability

The data supporting this study's findings can be obtained from the corresponding author upon reasonable request.

Author contributions

S. P., S. M., N. S. M. W., and A. P. developed the framework for the detection scheme and designed the experiments. N. S. M. W. carried out the sensor fabrication and conducted the experiments. Both N. S. M. W. and A. P. analysed the experimental data and collaborated on drafting the manuscript.

Conflicts of interest

Shalini Prasad and Sriram Muthukumar has a significant interest in EnLiSense LLC, a company that may have a commercial interest in the results of this research and technology. The potential individual conflict of interest has been reviewed and managed by The University of Texas at Dallas and played no role in the study design, in the collection, analysis, and interpretation of data; in the writing

of the report; or in the decision to submit the report for publication.

Acknowledgements

Notes and references

1 J. H. Wang, J. Byun and S. Pennathur, Analytical Approaches to Metabolomics and Applications to Systems Biology, *Semin. Nephrol.*, 2010, **30**(5), 500–511, DOI: **10.1016/j.semnephrol.2010.07.007**.

2 N. Lagopati, T. F. Valamvanos, V. Proutsou, K. Karachalios, N. Pippa, M. A. Gatou, I. A. Vagena, S. Cela, E. A. Pavlatou, M. Gazouli and E. Efstathopoulos, The Role of Nano-Sensors in Breath Analysis for Early and Non-Invasive Disease Diagnosis, *Chemosensors*, 2023, **6**, 317, DOI: **10.3390/chemosensors11060317**.

3 S. Qiu, Y. Cai, H. Yao, C. Lin, Y. Xie, S. Tang and A. Zhang, Small Molecule Metabolites: Discovery of Biomarkers and Therapeutic Targets, *Signal Transduction Targeted Ther.*, 2023, **8**, DOI: **10.1038/s41392-023-01399-3**.

4 K. Strimbu and J. A. Tavel, What Are Biomarkers?, *Curr. Opin. HIV AIDS*, 2010, 463–466, DOI: **10.1097/COH.0b013e32833ed177**.

5 A. Ahmad, M. Imran and H. Ahsan, Biomarkers as Biomedical Bioindicators: Approaches and Techniques for the Detection, Analysis, and Validation of Novel Biomarkers of Diseases, *Pharmaceutics*, 2023, **15**, 1630, DOI: **10.3390/pharmaceutics15061630**.

6 C. V. Berenguer, F. Pereira, J. A. M. Pereira and J. S. Câmara, Volatilomics: An Emerging and Promising Avenue for the Detection of Potential Prostate Cancer Biomarkers, *Cancers*, 2022, **14**, 3982, DOI: **10.3390/cancers14163982**.

7 A. S. Oyerinde, V. Selvaraju, J. R. Babu and T. Geetha, Potential Role of Oxidative Stress in the Production of Volatile Organic Compounds in Obesity, *Antioxidants*, 2023, **12**, 129, DOI: **10.3390/antiox12010129**.

8 V. Saasa, M. Beukes, Y. Lemmer and B. Mwakikunga, Blood Ketone Bodies and Breath Acetone Analysis and Their Correlations in Type 2 Diabetes Mellitus, *Diagnostics*, 2019, **9**(4), 224, DOI: **10.3390/diagnostics9040224**.

9 M. Khokhar, Non-Invasive Detection of Renal Disease Biomarkers through Breath Analysis, *J. Breath Res.*, 2024, **18**, DOI: **10.1088/1752-7163/ad15fb**.

10 P. Trefz, S. C. Schmidt, P. Sukul, J. K. Schubert, W. Miekisch and D. C. Fischer, Non-Invasive Assessment of Metabolic Adaptation in Paediatric Patients Suffering from Type 1 Diabetes Mellitus, *J. Clin. Med.*, 2019, **8**(11), 1797, DOI: **10.3390/jcm8111797**.

11 S. F. Solga, A. Alkhuraishe, K. Cope, A. Tabesh, J. M. Clark, M. Torbenson, P. Schwartz, T. Magnuson, A. M. Diehl and T. H. Risby, Breath Biomarkers and Non-Alcoholic Fatty Liver Disease: Preliminary Observations, *Biomarkers*, 2006, **11**(2), 174–183, DOI: **10.1080/13547500500421070**.

12 K. Dryahina, V. Pospíšilová, K. Sovová, V. Shestivska, J. Kubišta, A. Spesyvyi, F. Pehal, J. Turzíková, J. Votruba and P. Španěl, Exhaled Breath Concentrations of Acetic Acid Vapour in Gastro-Esophageal Reflux Disease, *J. Breath Res.*, 2014, **8**(3), DOI: **10.1088/1752-7155/8/3/037109**.

13 A. Singh, A. Sharma, A. Ahmed, A. K. Sundramoorthy, H. Furukawa, S. Arya and A. Khosla, Recent Advances in Electrochemical Biosensors: Applications, Challenges, and Future Scope, *Biosensors*, 2021, **11**, 336, DOI: **10.3390/bios11090336**.

14 I. Banga, A. Paul, D. C. Poudyal, S. Muthukumar and S. Prasad, Recent Advances in Gas Detection Methodologies with a Special Focus on Environmental Sensing and Health Monitoring Applications—A Critical Review, *ACS Sens.*, 2023, 3307–3319, DOI: **10.1021/acssensors.3c00959**.

15 S. T. Navale, Z. B. Yang, C. Liu, P. J. Cao, V. B. Patil, N. S. Ramgir, R. S. Mane and F. J. Stadler, Enhanced Acetone Sensing Properties of Titanium Dioxide Nanoparticles with a Sub-Ppm Detection Limit, *Sens. Actuators, B*, 2018, **255**, 1701–1710, DOI: **10.1016/j.snb.2017.08.186**.

16 S. Cao, N. Sui, P. Zhang, T. Zhou, J. Tu and T. Zhang, TiO2 Nanostructures with Different Crystal Phases for Sensitive Acetone Gas Sensors, *J. Colloid Interface Sci.*, 2022, **607**, 357–366, DOI: **10.1016/j.jcis.2021.08.215**.

17 Nagmani, D. Pravarthana, A. Tyagi, T. C. Jagadale, W. Prellier and D. K. Aswal, Highly Sensitive and Selective H2S Gas Sensor Based on TiO2 Thin Films, *Appl. Surf. Sci.*, 2021, **549**, DOI: **10.1016/j.apsusc.2021.149281**.

18 S. T. Navale, V. V. Jadhav, K. K. Tehare, R. U. R. Sagar, C. S. Biswas, M. Galluzzi, W. Liang, V. B. Patil, R. S. Mane and F. J. Stadler, Solid-State Synthesis Strategy of ZnO Nanoparticles for the Rapid Detection of Hazardous Cl2, *Sens. Actuators, B*, 2017, **238**, 1102–1110, DOI: **10.1016/j.snb.2016.07.136**.

19 M. Aleksanyan, A. Sayunts, V. Aroutiounian, G. Shahkhatuni, Z. Simonyan and G. Shahnazaryan, Gas Sensor Based on ZnO Nanostructured Film for the Detection of Ethanol Vapor, *Chemosensors*, 2022, **10**(7), 245, DOI: **10.3390/chemosensors10070245**.

20 M. Sik Choi, M. Young Kim, A. Mirzaei, H. S. Kim, S. i. Kim, S. H. Baek, D. Won Chun, C. Jin and K. Hyoung Lee, Selective, Sensitive, and Stable NO2 Gas Sensor Based on Porous ZnO Nanosheets, *Appl. Surf. Sci.*, 2021, **568**, DOI: **10.1016/j.apsusc.2021.150910**.

21 G. D. Khuspe, R. D. Sakhare, S. T. Navale, M. A. Chougule, Y. D. Kolekar, R. N. Mulik, R. C. Pawar, C. S. Lee and V. B. Patil, Nanostructured SnO2 Thin Films for NO2 Gas Sensing Applications, *Ceram. Int.*, 2013, **39**(8), 8673–8679, DOI: **10.1016/j.ceramint.2013.04.047**.

22 K. Gayathri, K. Ravichandran, M. Sridharan, S. Suvathi, S. Sriram, R. Mohan, A. Jansi Santhosam, P. K. Praseetha and P. Sakthivel, Enhanced Ammonia Gas Sensing by Cost-

Effective SnO2 Gas Sensor: Influence of Effective Mo Doping, *Mater. Sci. Eng., B*, 2023, **298**, DOI: **10.1016/j. mseb.2023.116849**.

23   S. T. Navale, C. Liu, P. S. Gaikar, V. B. Patil, R. U. R. Sagar, B. Du, R. S. Mane and F. J. Stadler, Solution-Processed Rapid Synthesis Strategy of Co3O4 for the Sensitive and Selective Detection of H2S, *Sens. Actuators, B*, 2017, **245**, 524–532, DOI: **10.1016/j.snb.2017.01.195**.

24   I. Banga, K. France, A. Paul and S. E. Prasad, Co Tech Breathalyzer: A Pilot Study of a Non-Invasive COVID-19 Diagnostic Tool for Light and Non-Smokers, *ACS Meas. Sci. Au*, 2024, **4**, 496–503, DOI: **10.1021/ acsmeasresciau.4c00020**.

25   I. Banga, A. Paul, A. U. Sardesai, S. Muthukumar and S. M. A. T. H. Prasad, Methanol Vapor Analytics through Handheld Sensing Platform, *Electrochim. Acta*, 2021, **368**, DOI: **10.1016/j.electacta.2020.137624**.

26   H. Wan, H. Yin and A. J. Mason, Rapid Measurement of Room Temperature Ionic Liquid Electrochemical Gas Sensor Using Transient Double Potential Amperometry, *Sens. Actuators, B*, 2017, **242**, 658–666, DOI: **10.1016/j. snb.2016.11.103**.

27   B. Kwon, H. Bae, H. Lee, S. Kim, J. Hwang, H. Lim, J. H. Lee, K. Cho, J. Ye, S. Lee and W. H. Lee, Ultrasensitive N-Channel Graphene Gas Sensors by Nondestructive Molecular Doping, *ACS Nano*, 2022, **16**(1), 2176–2187, DOI: **10.1021/ acsnano.1c08186**.

28   H. J. Yoon, D. H. Jun, J. H. Yang, Z. Zhou, S. S. Yang and M. M. C. Cheng, Carbon Dioxide Gas Sensor Using a Graphene Sheet, *Sens. Actuators, B*, 2011, **157**(1), 310–313, DOI: **10.1016/j.snb.2011.03.035**.

29   Y. S. Chang, F. K. Chen, D. C. Tsai, B. H. Kuo and F. S. Shieu, N-Doped Reduced Graphene Oxide for Room-Temperature NO Gas Sensors, *Sci. Rep.*, 2021, **11**(1), DOI: **10.1038/s41598-021-99883-9**.

30   L. Yang, G. Zheng, Y. Cao, C. Meng, Y. Li, H. Ji, X. Chen, G. Niu, J. Yan, Y. Xue and H. Cheng, Moisture-Resistant, Stretchable NOx Gas Sensors Based on Laser-Induced Graphene for Environmental Monitoring and Breath Analysis, *Microsyst. Nanoeng.*, 2022, **8**(1), DOI: **10.1038/ s41378-022-00414-x**.

31   M. Han, S. Jung, Y. Lee, D. Jung and S. Kong, PEI-Functionalized Carbon Nanotube Thin Film Sensor for CO2 Gas Detection at Room Temperature, *Micromachines*, 2021, **12**(9), 1053, DOI: **10.3390/mi12091053**.

32   S. M. Aalam, M. Sarvar, M. Sadiq and J. Ali, A Highly Sensitive Surface-Modified Porous Carbon Nanotube-Based Sensor for Ammonia Gas Detection, *ACS Omega*, 2024, **9**(4), 4486–4496, DOI: **10.1021/acsomega.3c07244**.

33   I. Banga, D. C. Poudyal, A. Paul, A. Sardesai, S. Muthukumar and S. Prasad, R.E.A.C.T-Rapid Electro-Analytical Graphitic Carbon Nitride-Based Screening Tool for Lung Cancer – Case Study Using Heptane, *Biosens. Bioelectron.:X*, 2023, **13**, DOI: **10.1016/j.biosx.2023.100311**.

34   H. Tian, H. Fan, M. Li and L. Ma, Zeolitic Imidazolate Framework Coated ZnO Nanorods as Molecular Sieving to Improve Selectivity of Formaldehyde Gas Sensor, *ACS Sens.*, 2016, **1**(3), 243–250, DOI: **10.1021/acssensors.5b00236**.

35   M. Zhan, C. Ge, S. Hussain, A. S. Alkorbi, R. Alsaiari, N. A. Alhemiary, G. Qiao and G. Liu, Enhanced NO2 Gas-Sensing Performance by Core-Shell SnO2/ZIF-8 Nanospheres, *Chemosphere*, 2022, **291**, DOI: **10.1016/j. chemosphere.2021.132842**.

36   I. Banga, A. Paul, A. Sardesai, S. Muthukumar and S. Prasad, AuNP@ZeNose (ZIF-Based Electrochemical Nose) for Detection of Flu Biomarker in Breath, *Microchim. Acta*, 2022, **189**(6), DOI: **10.1007/s00604-022-05334-1**.

37   I. Banga, A. Paul, S. Muthukumar and S. Prasad, ZENose (ZIF-Based Electrochemical Nose) Platform for Noninvasive Ammonia Detection, *ACS Appl. Mater. Interfaces*, 2021, **13**(14), 16155–16165, DOI: **10.1021/acsami.1c02283**.

38   M. N. Padvi, A. V. Moholkar, S. R. Prasad and N. R. Prasad, A Critical Review on Design and Development of Gas Sensing Materials, *Eng. Sci.*, 2021, 20–37, DOI: **10.30919/es8d431**.

39   T. Han, A. Nag, S. Chandra Mukhopadhyay and Y. Xu, Carbon Nanotubes and Its Gas-Sensing Applications: A Review, *Sens. Actuators, A*, 2019, 107–143, DOI: **10.1016/j. sna.2019.03.053**.

40   H. Nazemi, A. Joseph, J. Park and A. Emadi, Advanced Micro-and Nano-Gas Sensor Technology: A Review, *Sensors*, 2019, **19**, 1285, DOI: **10.3390/s19061285**.

41   V. Gargiulo, M. Alfè, L. Giordano and S. Lettieri, Materials for Chemical Sensing: A Comprehensive Review on the Recent Advances and Outlook Using Ionic Liquids, Metal–Organic Frameworks (MOFs), and MOF-Based Composites, *Chemosensors*, 2022, **10**, 290, DOI: **10.3390/ chemosensors10080290**.

42   V. S. Bhati, M. Kumar and R. Banerjee, Gas Sensing Performance of 2D Nanomaterials/Metal Oxide Nanocomposites: A Review, *J. Mater. Chem. C*, 2021, 8776–8808, DOI: **10.1039/d1tc01857d**.

43   P. K. Panigrahi, B. Chandu and N. Puvvada, Recent Advances in Nanostructured Materials for Application as Gas Sensors, *ACS Omega*, 2024, **3**, 3092–3122, DOI: **10.1021/ acsomega.3c06533**.

44   R. Zhang, L. Lu, Y. Chang and M. Liu, Gas Sensing Based on Metal-Organic Frameworks: Concepts, Functions, and Developments, *J. Hazard. Mater.*, 2022, **429**, DOI: **10.1016/j. jhazmat.2022.128321**.

45   S. M. Majhi, A. Ali, P. Rai, Y. E. Greish, A. Alzamly, S. G. Surya, N. Qamhieh and S. T. Mahmoud, Metal-Organic Frameworks for Advanced Transducer Based Gas Sensors: Review and Perspectives, *Nanoscale Adv.*, 2022, 697–732, DOI: **10.1039/d1na00798j**.

46   A. Paul, I. K. Banga, S. Muthukumar and S. Prasad, Engineering the ZIF-8 Pore for Electrochemical Sensor Applications-A Mini Review, *ACS Omega*, 2022, 26993–27003, DOI: **10.1021/acsomega.2c00737**.

47   I. Banga, A. Paul, S. Muthukumar and S. Prasad, ZENose (ZIF-Based Electrochemical Nose) Platform for Noninvasive Ammonia Detection, *ACS Appl. Mater. Interfaces*, 2021, **13**(14), 16155–16165, DOI: **10.1021/acsami.1c02283**.

48 J. Qin, M. Cho and Y. Lee, Ferrocene-Encapsulated Zn Zeolitic Imidazole Framework (ZIF-8) for Optical and Electrochemical Sensing of Amyloid-β Oligomers and for the Early Diagnosis of Alzheimer's Disease, *ACS Appl. Mater. Interfaces*, 2019, **11**(12), 11743–11748, DOI: **10.1021/acsami.8b21425**.

49 A. Paul, G. Vyas, P. Paul and D. N. Srivastava, Gold-Nanoparticle-Encapsulated Zif-8 for a Mediator-Free Enzymatic Glucose Sensor by Amperometry, *ACS Appl. Nano Mater.*, 2018, **1**(7), 3600–3607, DOI: **10.1021/acsanm.8b00748**.